Non-invasive measurement of brown fat metabolism based on optoacoustic imaging of hemoglobin gradients.

Josefine Reber[1,#], Monja Willershäuser[2,#], Gael Diot[1], Angelos Karlas[1], Daniela Franz[4], Dimitrios C. Karampinos[4], Tobias Fromme[2], Saak V. Ovsepian[1], Nicolas Bézière[1], Elena Dubikovskaya[5], Christina Holzapfel[3], Hans Hauner[3], Martin Klingenspor[2], Vasilis Ntziachristos[1,*]

[1]*Institute for Biological and Medical Imaging (IBMI), Helmholtz Zentrum München, Ingolstädter Landstr. 1, 85764 Neuherberg & Chair for Biological Imaging, Technical University Munich, Trogerstrasse. 9, 81675 München, Germany*

[2]*Chair for Molecular Nutritional Medicine, Technical University Munich, Else Kröner-Fresenius Center for Nutritional Medicine, Gregor-Mendel-Str. 2, 85350 Freising, & Z I E L – Institute for Food and Health, Technical University Munich, Gregor-Mendel-Str. 2, 85350 Freising, Germany;*

[3]*Institute for Nutritional Medicine, Faculty of Medicine, Technical University Munich, Georg-Brauchle-Ring 62, 80992 Munich, & Z I E L – Institute for Food and Health, Technical University Munich, Gregor-Mendel-Str. 2, 85350 Freising, Germany*

[4]*Department of Diagnostic and Interventional Radiology, Technical University Munich, Ismaninger Str. 22, 81675 Munich, Germany;*

[5]*Department of Chemistry, Ecole Polytechnique Federale de Lausanne, 1015 Lausanne, Switzerland*

[#]*Equally contributing authors*

**Corresponding author:*

Vasilis Ntziachristos, Ph.D., Professor
Chair for Biological Imaging
Technical University Munich
Ismaningerstr. 22, 81675 München
Germany
Phone: 49-89-31873852
Fax: 49-89-3187173852
E-mail: v.ntziachristos@tum.de

Key words: Optoacoustic (photoacoustic), indirect calorimetry, brown adipose tissue, blood oxygenation, multispectral optoacoustic tomography, positron emission tomography

Abstract

Metabolism is a fundamental process of life. However, non-invasive imaging of tissue metabolism is limited today by a deficiency in adequate tools for *in vivo* measurements. We designed a novel multi-modular platform that explored the relation between local tissue oxygen consumption, determined by label-free optoacoustic measurements of hemoglobin, and concurrent indirect calorimetry obtained during metabolic activation of brown adipose tissue (BAT). By studying mice and humans, we show how recent technological advances in video-rate handheld multi-spectral optoacoustic tomography (MSOT) in the 700-900 nm spectral range enable non-invasive imaging of BAT activation and metabolic state based on hemoglobin gradients. We find that indirect calorimetry may under-estimate local metabolic activation compared to MSOT measurements. We further observe BAT morphology and composition differences between healthy and diabetic mice. Human measurements, validated by Positron Emission Tomography, consolidate hemoglobin as a principal label-free biomarker for longitudinal non-invasive imaging of lipid and tissue metabolism, as well as bioenergetics *in situ*, with broad implications for basic and translational research. In addition to hemoglobin, we further resolve water and fat components in healthy volunteers, using 28 wavelength illumination at an extended 700-970 nm spectral region and contrast results to Magnetic Resonance Imaging (MRI). We discuss the superiority of MSOT to assess tissue metabolism over available methods.

Introduction

White adipose tissue (WAT) stores in its cellular fat droplets a surplus of vital energy consisting of macronutrients mainly in the form of triacylglycerides. In contrast, brown adipose tissue (BAT) works as a heater organ, utilizing the chemical energy extracted from carbohydrates and fat (1, 2). The presence of metabolically active cervical, supraclavicular, and paravertebral BAT in adult humans has been discovered by the detection of high glucose uptake rates using positron emission tomography (^{18}F-FDG-PET/CT) (3, 4). In mice, BAT is located in several distinct depots in the cervical-thoracic and perirenal region and is utilized for non-shivering thermogenesis (1, 5). The largest and most investigated BAT depot in rodents is the subcutaneous interscapular BAT (iBAT). It is densely vascularized and highly innervated by the sympathetic nervous system (6, 7). Research in small mammals has shown that cold exposure leads to the release of norepinephrine (NE) from nerve varicosities. The neurotransmitter NE stimulates β3-adrenoreceptors located in the plasma membrane of brown adipocytes, resulting in the activation of the uncoupling protein 1 (UCP1) (1). UCP1 is expressed uniquely in brown adipocytes and upon activation facilitates a proton leak across the mitochondrial inner membrane, leading to the uncoupling of nutrient oxidation from ATP synthesis and thereby to heat generation (2, 8). BAT can also be activated via the subcutaneous or intravenous injection of sympathomimetics at the optimal dose, whereby the maximal increase of total resting metabolic rate is used as a direct measure of BAT heating capacity (9, 10). Sympathetic stimulation, however, not only activates BAT-induced non-shivering thermogenesis, but also increases energy expenditure at other sites, e.g. the cardiovascular system, potentially leading to an overestimation of BAT-induced thermogenesis (1).

The study of BAT physiology has attracted attention in recent years, due to the assumed association of BAT with a wide variety of human diseases such as obesity (low BAT activity), diabetes (absence of active BAT), cachexia (high amount and activity of BAT) and atherosclerosis (atheroprotective role of BAT and similar perivascular fat) (11). Classic studies obtained snapshots of BAT metabolic activity by measurements of blood flow, as assessed by injecting radiolabelled

particles, and arterio-venous differentials in blood oxygenation (12-14). Non-invasive ^{18}F-FDG-PET imaging resolves glucose uptake rates in living tissue but underestimates metabolic activity of BAT (11, 15), since thermogenesis is largely fueled by mitochondrial beta-oxidation of fatty acids. ^{18}F-FTHA and ^{11}C-acetate may address this issue (see e.g. Ouellet et al (16)), but the use of radio-isotopes does not allow continuous or longitudinal studies and is problematic for human measurements. Studies with functional magnetic resonance imaging (fMRI) (17) or near-infrared (NIR) fluorescence imaging (18) have provided observations of blood flow associated with BAT activation but did not accurately differentiate BAT from WAT. Likewise, infrared imaging has been considered for resolving local temperature changes after BAT activation (19), but it provides two-dimensional views of volumetric temperature changes within the examined tissue volume, which has not resulted in an accurate surrogate measure of metabolism. The study of BAT and other tissue metabolism could be revolutionized by methods that offer non-invasive and point-of-care longitudinal measurements of activity, avoiding radioactivity or the use of targeted contrast agents and expensive scanners and infrastructure. Such technology could promote the disseminated investigation of metabolism in BAT and other tissue over time and in response to external natural stimuli or new anti-obesity drugs in animals and humans in a personalized manner.

We investigated *label-free* non-invasive imaging of BAT activation and tissue metabolic activity based on real-time NIR optoacoustic sensing of hemoglobin. Label-free imaging based on non-ionizing energy avoids the use of contrast agents and opens up the possibility for frequent and longitudinal measurements in individual subjects. A primary hypothesis in the study was that BAT activation could be measured by resolving hemoglobin oxygenation gradients, representative of local oxygen utilization and blood influx.

To validate hemoglobin gradients as a marker of energy expenditure we developed an experimental arrangement that concurrently collected multi spectral optoacoustic tomography (MSOT) and breathing gas data from mice and humans, using indirect calorimetry (IC). Necessary imaging

performance was achieved based on a unique imaging sequence, which collected one cross-sectional optoacoustic image per laser pulse and per wavelength at 10Hz frame rates over a 700nm-970nm spectral range. Up to 28 illumination wavelengths per MSOT frame were collected. Previously undisclosed correlation of indirect calorimetry with *in situ* MSOT measurements of BAT metabolic changes was performed in mice and pilot studies in humans. Human findings were further corroborated using ^{18}F-FDG-Positron Emission Tomography (PET).

In addition to BAT activation studies, we investigated morphological discrimination between BAT and WAT in healthy and diabetic mice. While hemoglobin can be unmixed in the 700-900 nm range, MSOT operation in the extended 900-970 nm range further computed tissue fat and water components in human volunteer studies and observed tissue composition differences in BAT and WAT, contrasted to Magnetic Resonance Imaging (MRI) of the same volunteers. We discuss how MSOT demonstrates capacities in metabolic imaging that are unattainable by any other imaging modality today, offering a paradigm shift in the study of metabolic processes in living tissue. Shown correlation between MSOT measurements of local metabolic activity and indirect calorimetry measuring whole body metabolic profiles may have broad implications in metabolism research and clinical applications in obesity, diabetes, atherosclerosis and related fields.

Results

Optoacoustic differentiation of BAT from WAT

We interrogated whether iBAT and inguinal WAT (ingWAT) can be spectrally differentiated. We were particularly interested in NIR measurements that allow light penetration several millimeters to centimeters deep in tissue. Excised iBAT and ingWAT from mice were placed next to an India Ink reference tube in a scattering (non-absorbing) holder and measured by NIR-MSOT under identical conditions (Fig. 1a; see experimental arrangement in **suppl. Fig. S1a**). At 800 nm the mean pixel intensity of the 2D transverse optoacoustic image of iBAT was 103 ± 13 a.u., whereby ingWAT was at

42 ± 7 a.u. and the reference absorber at ~64 a.u. in all measurements. When comparing the spectra of iBAT, ingWAT and black India ink (OD=0.5 at 800 nm), iBAT showed the overall highest signal intensity (light absorption) with a local maximum at 750 nm and a minimum at 830 nm. IngWAT has a maximum at 740 nm and a minimum at 800 nm. As expected, India Ink demonstrated the highest absorption in the 700 nm region and a gradual absorption decrease toward 900 nm (Fig. 1b).

To inquire whether iBAT can be separated from ingWAT and other surrounding tissues *in vivo*, we imaged nude mice by MSOT in the NIR range (700 – 900 nm). iBAT is typically localized in the cervical-thoracic region as shown in an anatomical transverse cryoslice (Fig. 1c) obtained by white-light (color) imaging of cryo-slices from a mouse enrolled in the MSOT imaging study. The iBAT depot resides between the shoulder blades of the animal in a bilateral symmetrical arrangement, on the left and right of the body axis. Mice were anesthetized using pentobarbital, which has no inhibitory effects on BAT thermogenesis (17, 22), in contrast to isoflurane and other inhalation anesthetics including halothane (23-25). An optoacoustic image at 800 nm exhibited areas with strong absorption (Fig. 1d) that were congruent with the areas identified as iBAT in the corresponding cryoslice (Fig. 1c). The ingWAT spectrum collected *in vivo* is flat when compared to the iBAT spectrum also *in vivo* (Fig. 1e); the latter has a minimum at 760 nm and a maximum at 800 nm. In addition to the spectral differences, iBAT exhibits a stronger optoacoustic signal than surrounding tissues *in vivo*, which allows the visualization of iBAT even at a single wavelength. Thus, the results demonstrate that MSOT can differentiate BAT and WAT morphology *ex vivo* and *in vivo*. MSOT also allowed the anatomical capture of the Sulzer vein (SV: Fig. 1e black square; see also Fig. 2a and Fig. 3a), representing the main venous drainage of iBAT.

The iBAT content in streptozotocin-induced diabetic male Balb/c mice (n=3) was also interrogated and compared to the one in healthy controls (n=3). MSOT identified a discrete but lower mean signal within the iBAT region of interest (ROI) of diabetic mice, compared to healthy mice (Fig.1 f,g; **suppl. Fig. 2S and suppl. Table S1**). This observation is consistent with findings in ^{18}F-

FDG microPET studies (26). We further separated the contributions of oxygenated hemoglobin (HbO_2) and deoxygenated hemoglobin (Hb), based on their characteristic absorption spectra using spectral processing of the MSOT images. The HbO_2 and Hb in the iBAT of diabetic mice were found to be 0.22 ± 0.01 and 0.18 ± 0.01, respectively. In heathy control animals, higher HbO_2 and Hb values were measured (HbO_2: 0.45 ± 0.02; Hb: 0.29 ± 0.01; see **suppl. S2 a**). Images are in all cases normalized to the signal of an artery, assumed to contain 100% HbO_2.

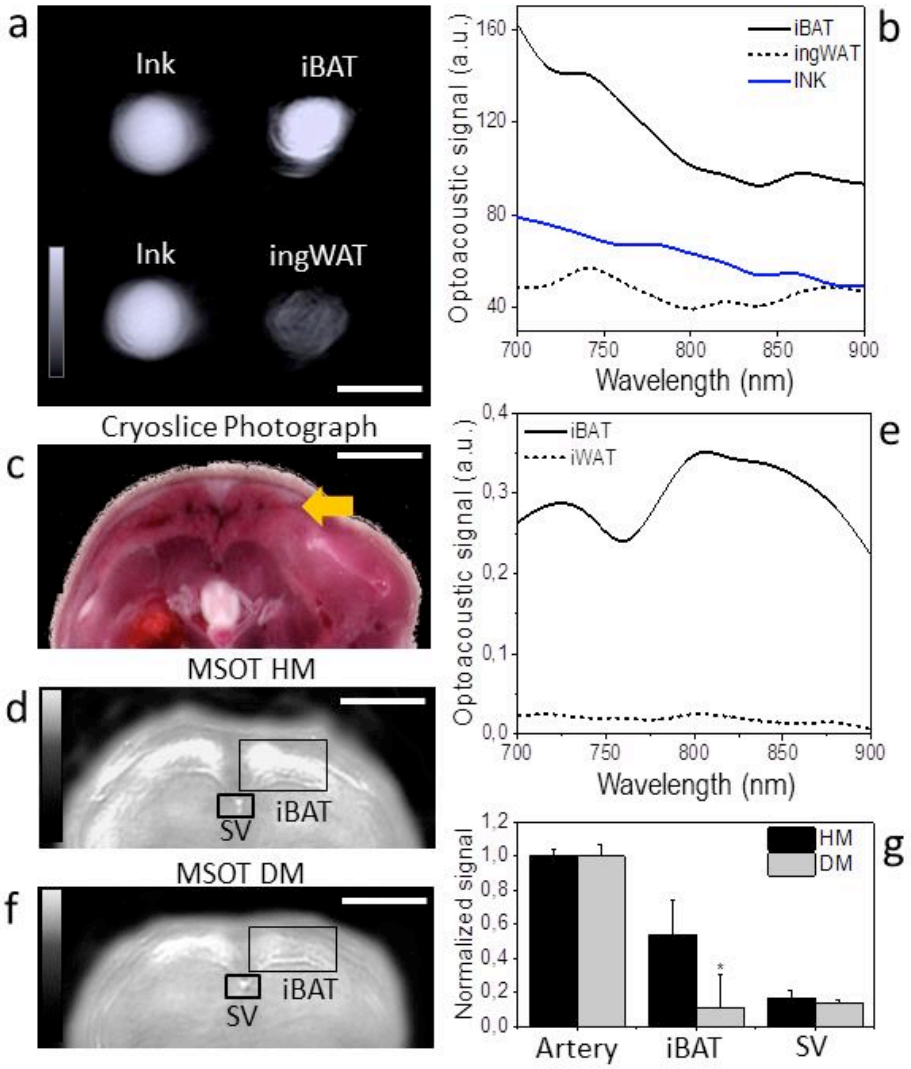

Figure 1: *Ex vivo* and *in vivo* comparison of the optoacoustic signal generated from iBAT and ingWAT. (a) Reconstructed optoacoustic images of excised iBAT and ingWAT from PFA-perfused animals and ink (OD=0.5 at 800 nm) measured at 800 nm in scattering phantom. (b) Optoacoustic spectra of *ex vivo* iBAT, ingWAT and ink in the NIR as measured by MSOT. (c) Anatomical transverse cryoslice of the neck area showing iBAT. (d) Reconstructed MSOT image (800 nm) showing iBAT and the Sultzer vein (SV) *in vivo* (black squares). (e) Optoacoustic spectra of *in vivo* iBAT, ingWAT in the NIR region as measured by MSOT. (f) Reconstructed MSOT image (800 nm) of diabetic mouse (DM) *in vivo.* (g) Normalized signal of MSOT image (800 nm) in a reference artery, the iBAT and SV in healthy mouse (HM) and DM. Scale bars; 3 mm (a),1 cm (b, d, f). (*$p < 0.05$).

In vivo imaging of iBAT activation in mouse

Next, we examined the possibility to interrogate iBAT activation in healthy mice based on measurements of oxygenated and deoxygenated hemoglobin gradients, hypothesized herein as an intrinsic biomarker of metabolism. We developed a novel experimental platform for performing, for the first-time reported, a correlation of hemoglobin-based optoacoustic readings to concurrent indirect calorimetry (IC) measurements based on breathing gas analysis (FoxBox, Sable Systems International, USA) (**suppl. Fig. S1a**). iBAT activation was induced in nude mice (n=6) by intravenous administration (1 mg/kg) of norepinephrine (NE).

Baseline (pre-NE) and iBAT activation (post-NE) MSOT images were recorded over a period of 42 minutes with a step of ~4 min, resulting in 4 iBAT pre-NE scans and 7 post-NE scans. At baseline, MSOT clearly identified two bilaterally symmetrical iBAT locations (Fig. 2a) which were subsequently employed to define regions of interest (ROI's) for HBO_2 and Hb calculations. Unmixed HBO_2 (Fig.2c) and Hb (Fig.2d) images identified mean HbO_2 intensity of the iBAT ROI of 0.45 ± 0.07 prior to activation and 0.96 ± 0.08 after activation ($p < 0.0001$). The Hb signal intensity increased significantly from 0.34 ± 0.06 to 0.64 ± 0.08 ($p < 0.0001$) (Fig. 2b). As in the experiments above, values are referenced to an artery signal, i.e. to a 100% HbO_2 signal. Intensity profiles drawn through the iBAT regions along the cross-sectional black dashed line marked with the term "profile" on Fig. 2a demonstrated intensity differences between baseline and activated states for the bilateral iBAT lobes but not for surrounding tissues (Fig. 2e,f). Area under the curve (AUC) calculations for the HbO_2 profiles (Fig. 2e) identified an AUC change from 30.8 ± 6.1. (NE-) to 63.6 ± 2.6 (NE+) after activation ($p = 0.007$). The AUC of the Hb profile (Fig. 2f) was 20.1 ± 3.7 (NE-) before and 39.2 ± 1.8 (NE+) after activation ($p = 0.027$). To quantify the spatial topology of the activation, we drew contour maps (**suppl. Fig. S3 a,c**) of the HbO_2 and Hb spatial patterns observed *in vivo* for the ROI. The contours quantify the areas implicated in the activation and demonstrate a 3.6-fold mean increase of high-intensity areas for HbO_2 and a 2.1-fold mean increase for Hb within iBAT between pre-NE and post-NE measurements for the mice examined (**see suppl. Fig. S3**).

Longitudinal imaging of the HbO_2 and Hb in iBAT show well-resolved changes in HbO_2 and Hb signals during activation and reveal a maximum change at ~1200 sec after NE administration in iBAT (Fig. 2g,h). HbO_2 and Hb signals from the iBAT ROIs were compared to oxygen consumption ($\dot{V}O_2$) measured by IC over time (Fig. 2i). The HbO_2 and $\dot{V}O_2$ response occurred virtually immediately after NE administration, whereas changes in the Hb signal appeared in a delayed fashion. Approximately 500 sec after NE administration, the HbO_2 signal dropped, indicating a surge of oxygen utilization, whereas the Hb signal exhibited only a small change. At 700 sec after NE administration there is a prominent increase in both HbO_2 and Hb signals, indicating a blood volume increase (blood flow/perfusion) in the activated iBAT area. $\dot{V}O_2$ was found to increase from 38 ± 5 ml/h at baseline to 73 ± 11 ml/h after activation ($p = 0.002$). Minor changes in response to NE were measured in WAT and muscle (Fig. 2j). Control mice, injected with saline at the same time point as the NE injection, showed no significant difference ($\dot{V}O_2$: 42 ± 4 ml/h at baseline and 43 ± 5 ml/h at post-injection, $p = 0.3$; HbO_2: 0.43 ± 0.04 at baseline and 0.49 ± 0.11 at post-injection, $p = 0.3$; Hb: 0.35 ± 0.03 at baseline and 0.36 ± 0.05 at post-injection, $p= 0.5$) (**suppl. Fig. S3**). We further studied the derivative of HbO_2 and Hb (Fig. 2k,l), which indicates the rate of change in blood constituent levels, reflecting their utilization and transport in tissue. The maximum HbO_2 rate occurred at 750 sec and the maximum Hb rate at 1000 sec after activation. The correlation between hemoglobin and IC measurements confirms the original hypothesis that high-resolution images of HbO_2 and Hb reflect BAT activation. However, in contrast to IC measurements, MSOT readings allow *in situ* observations along with the visualization of the metabolically activated area.

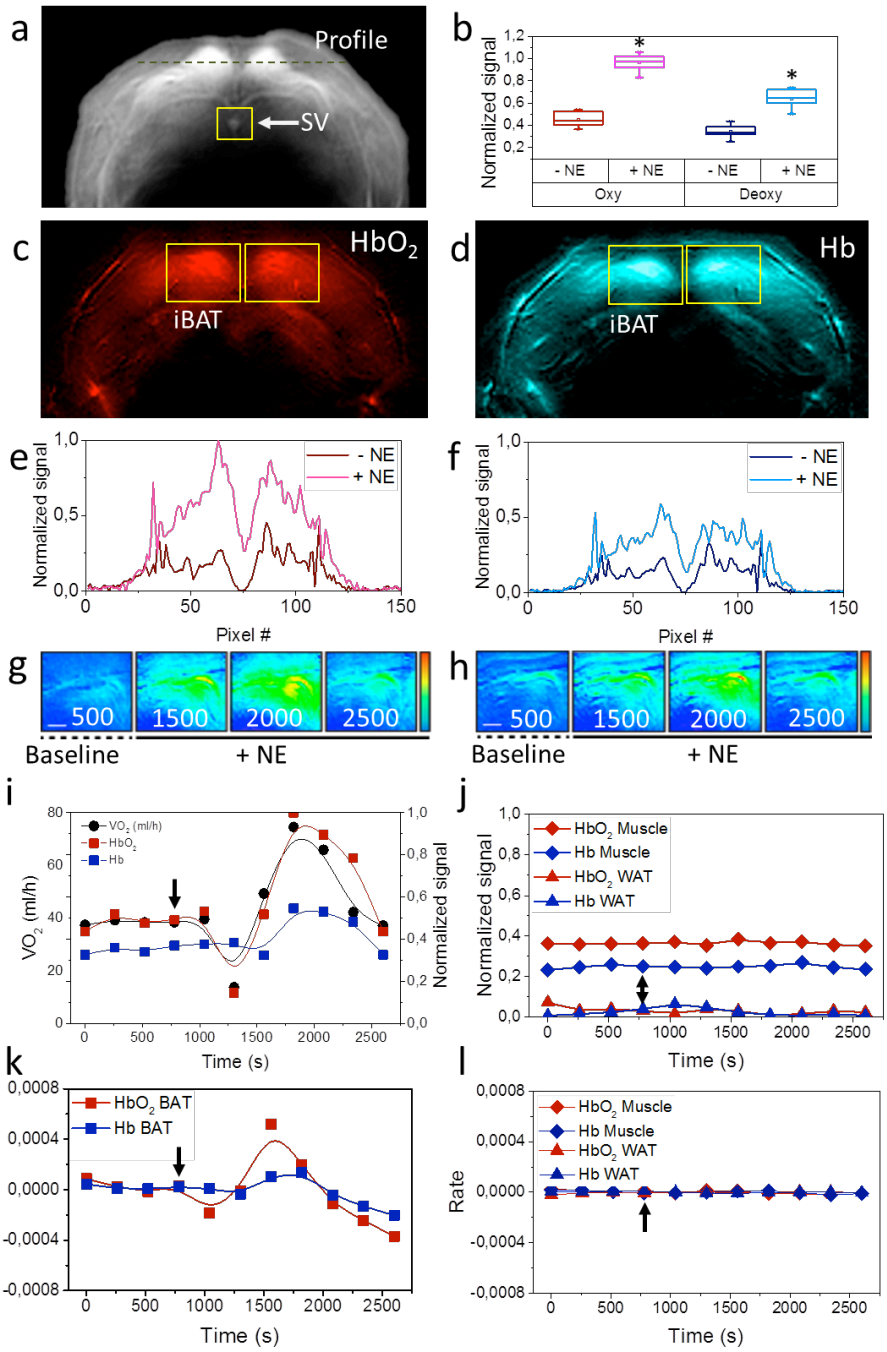

Figure 2: O_2 consumption and oxygenation status measurements during iBAT activation. (a) Anatomical image at 800 nm showing the iBAT profile and the Sulzer vein (SV). (b) Boxplot of the normalized signal intensity of oxygenated (HbO_2) and deoxygenated (Hb) hemoglobin in the ROI of iBAT of animals analyzed. (c) MSOT image of the right iBAT lobe of an animal, illustrating the intensity of HbO_2 after activation of BAT with NE. The corresponding horizontal intensity profile is shown in (e). (d) MSOT image of the right iBAT lobe of an animal illustrating the intensity of Hb after activation of iBAT with NE. The corresponding horizontal intensity profile is shown in (f). (g,h) Time course of HbO_2 and Hb imaging differences from baseline. (i) Time course of O_2 consumption ($\dot{V}O_2$) and changes in HbO_2 and Hb before and after iBAT activation with NE. Injection time point indicated with a black arrow. (j) Time course of changes in HbO_2 and Hb in muscle and WAT before and after iBAT activation with NE. Injection time point indicated with a black arrow. (k,l) Time derivatives (rates of change) of HbO_2 and Hb, indicative of HbO_2 or Hb utilization. Scale bars; 1.0 mm (g,h). (*$p < 0.05$).

Saturation and Blood volume rates

The sum of HbO_2 and Hb, defined as total blood volume (TBV), and the fractional contribution of HbO_2 normalized against the TBV, i.e. the blood oxygen tissue saturation (SO_2), were also calculated (Fig. 3a,b) based on MSOT images and are shown here to have a different time response than their Hb and HbO_2 constituents. After NE administration, SO_2 initially decreases, possibly because of higher metabolic demand, and then increases to a maximum at ~1000 sec post-NE. TBV follows a similar trend, starting to increase at ~850 sec post-NE (Fig. 3c,d). Time derivatives of SO_2 and TBV values were also computed, since while SO_2 values indicate the amount of HbO_2 in the total blood volume present in tissue, the rate of SO_2 change more closely reflects oxygen demand by tissue, i.e. oxygen utilization. Observation of the SO_2 rate (time derivative; Fig. 3 e) indicates an increase in oxygen demand (metabolism) immediately after NE activation, which intensifies in the subsequent ~700 seconds post-activation. The TBV rate (Fig. 3f) also indicates an increased demand in blood volume and is representative of the blood volume influx, i.e. flow or perfusion.

To independently assess oxygen utilization, we spectrally resolved oxygenated and deoxygenated hemoglobin within the lumen of the Sulzer vein (SV; see Fig. 1d, Fig. 2a, Fig. 3a) before and after activation and calculated the SO_2 and TBV, respectively (Fig. 3g,h). We observed that SO_2 dropped significantly at ~1250 sec after NE activation in the SV from 70 ± 15 % to 55 ± 16 % ($p = 0.0008$, Fig. 3i). The optoacoustic signals reporting TBV in SV increased significantly after activation from 0.14 ± 0.03 to 0.20 ± 0.05 ($p = 0.0002$, Fig. 3j). No changes in SO_2 and TBV were observed in the SV of control animals injected with saline (data not shown). On the contrary, at the maximum of activation (~1250 sec after NE injection) we observed significant increases of SO_2 and TBV in the bilateral iBAT lobes (SO_2: 81 ± 13 % at baseline and 95 ± 14 % after activation, $p < 0.0001$; TBV: 0.58 ± 0.14 baseline and 1.04 ± 0.16 after activation, $p= 0.0004$). In an artery used as reference (indicated with a white box), neither the SO_2 nor the TBV increased significantly. These findings demonstrate that SO_2 and TBV gradients in BAT and in the SV can be resolved in mouse and indicate metabolic activity. SO_2 gradients could be regarded as indicative of metabolic demand (oxygen utilization), whereas TBV changes indicate change in blood flow/perfusion of the area

observed. This feature may lead to better quantification of relative activation changes in the study of metabolism *in vivo*.

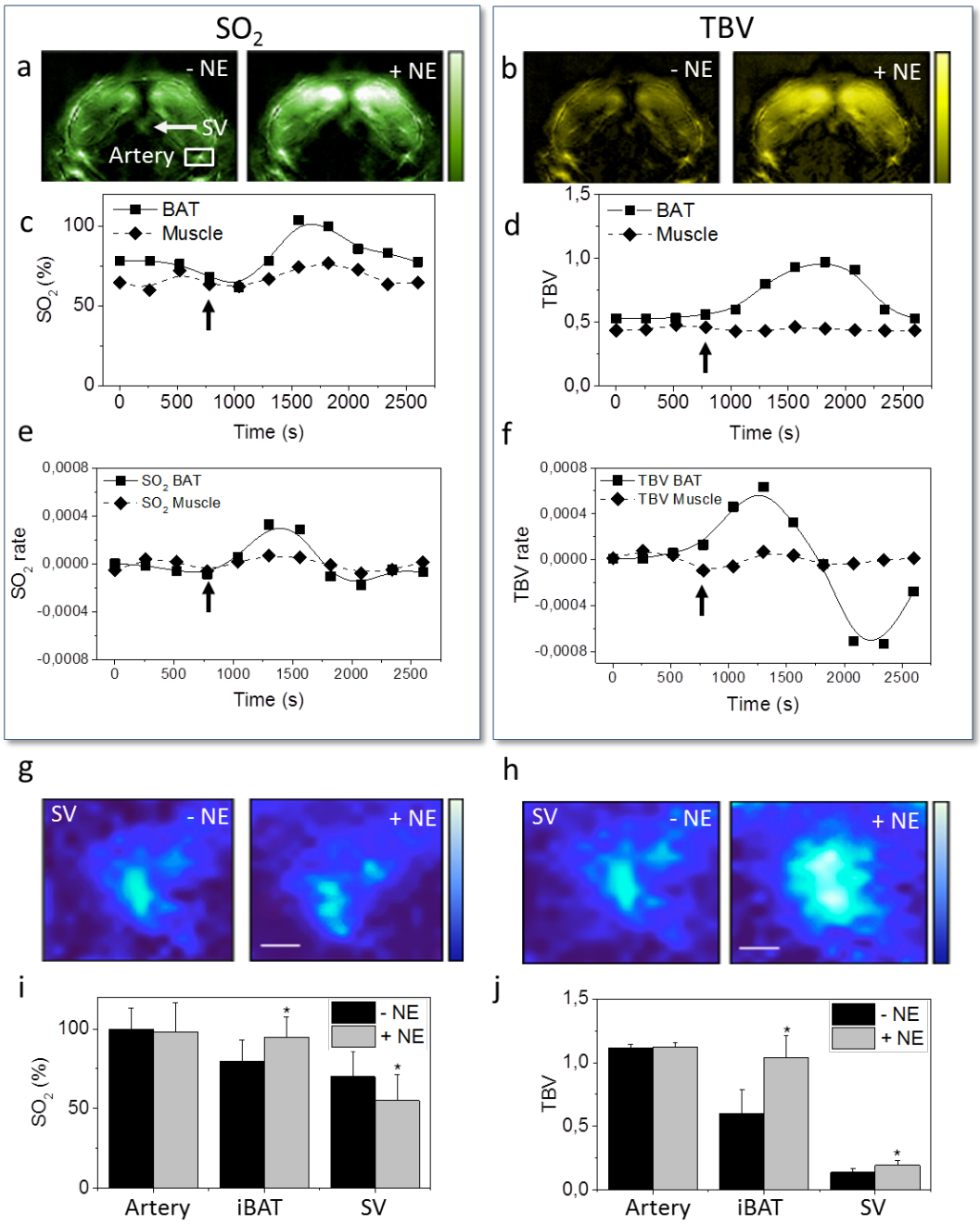

Figure 3: Optoacoustic assessment of changes in blood oxygen saturation (SO_2) and total blood volume (TBV) before and after iBAT activation with NE in mouse. (a) MSOT image of SO_2 before and after NE injection. (b) MSOT image of TBV before and after NE injection. (c) Time course of SO_2 in iBAT and muscle. Injection of norepinephrine (NE) is indicated with a black arrow. (d) Time course of TBV in iBAT and muscle. Injection of norepinephrine is indicated with a black arrow. (e) Rate of SO_2 time curve in iBAT and muscle. (f) Rate of TBV time curve in iBAT and muscle. (g) MSOT images of relative changes in SO_2 before and after NE injection. (h) MSOT images of relative changes in TBV before and after NE injection. (i) Normalized signal of SO_2 in a reference artery, iBAT and SV before and after activation with NE. (j) Normalized signal of TBV in a reference artery, iBAT and SV before and after activation with NE. Scale bars, 0.2 mm (g,h). (*$p < 0.05$).

297 *MSOT handheld measurements and indirect calorimetry in human subjects*

298 The neck and the supraclavicular region of volunteers (n=3) that displayed ^{18}F-FDG uptake in
299 BAT were imaged using video-rate handheld MSOT (**suppl. Fig. S1b**), to interrogate whether BAT
300 could be optoacoustically measured in humans (Fig. 4 a-f). Oblique slices (Fig. 4b,c) were extracted
301 from volumetric PET images co-registered with MRI images (Fig. 4a). MRI (Fig. 4d) and co-
302 registered MRI-PET slices (Fig. 4e) of the supraclavicular region (i.e. the region of interest outlined
303 with a yellow dotted-line box on Fig. 4c) were used to validate corresponding MSOT images (Fig. 4f)
304 obtained from the same region. Since PET resolution is ~9 mm, MRI oblique resolution is ~3 mm and
305 MSOT resolution ~0.3 mm, the MSOT oblique-slice image (Fig. 4f) gives a more detailed view of the
306 tissue than oblique PET or oblique MRI. The MSOT image captures information corresponding to a
307 triangular muscle structure, enclosed by the outer skin boundary and the dotted line in image Fig. 4f,
308 which is also visible in the oblique MR image (Fig. 4d) albeit with much lower resolution. On the
309 anterior side of the muscle lies metabolically active adipose tissue (white arrow; Fig. 4f), identified on
310 the PET-MRI images (Fig. 4a, Fig. 4d,e) as a BAT region.

311 In a next step, activation was induced via cold exposure of the whole body by means of a suit
312 perfused with 13°C cold water (n=3). IC measurements of oxygen consumption were conducted in
313 parallel to the MSOT measurements for validation purposes (Fig. 4g), using an exercise physiology kit
314 (ML3508B80 Exercise Physiology System, ADInstruments, NZ). MSOT images obtained before and
315 after cold exposure. BAT images (Fig. 4h) obtained from the area marked with a white arrow on Fig.
316 4f exhibited higher optoacoustic signal after activation than the areas from the muscle region indicated
317 by the green arrow on Fig. 4f. Other vascular structures within BAT tissue and at the interface
318 between BAT and the surrounding muscle regions also exhibited post-activation signal changes
319 (**suppl. Fig. S4c,d**).

320 Similarly to the animal measurements, the HbO_2 signal intensity from BAT correlated with the
321 corresponding $\dot{V}O_2$ measurements (Fig. 4i). The HbO_2 intensity in the BAT region changed
322 significantly with cold activation (0.34 ± 0.12 at baseline vs. 0.92 ± 0.08 after cooling, $p = 0.004$),
323 whereas no significant activity was captured from the muscle region (0.29 ± 0.09 at baseline and 0.37

± 0.08 after cooling, p = 0.09). Small signal variations were observed in the skin (0.98 ± 0.04 at baseline and 1.16 ± 0.04 after cooling, p = 0.05) (Fig. 4j). In contrast to muscle and BAT, which are illuminated with diffusive light, the skin receives concentrated light energy. Therefore such changes could be at least partially explained as small thermal effects, in analogy to the animal measurements. The percentage change in three individuals showed that the optoacoustic signal in the muscle changes 1 ± 2 %, whereby the $\dot{V}O_2$ changes 4.5 ± 1 % and the optoacoustic signal in the BAT changes 372 ± 105 % (Fig. 4k). This is in accordance with the findings of SO_2 and TBV, which show a clear increase in BAT but not in muscle after cooling (**suppl. Fig. 4a,b**). Thus, the results demonstrate that MSOT can optoacoustically detect BAT and activation in humans.

Hemoglobin, fat and water MSOT features in human volunteers

In a final step we examined the imaging features of human BAT vs. WAT provided by MSOT. Optoacoustic imaging was performed by illuminating the supraclavicular region of 26 volunteers in the 700-970 nm spectral region and unmixed in this case four tissue components, i.e. fat and water in addition to Hb and HbO_2. Spectrally, fat and water absorb primarily in the 900-970nm spectral region, whereby hemoglobins absorb primarily in the 700-900 nm spectral window. All volunteers were also imaged by a multi-echo gradient echo MRI sequence in a 3T clinical scanner (see methods for details).

Transverse tomographic MR Proton Density Fat Fraction (PDFF) maps were obtained from the shoulder region of the volunteers (see **suppl. Fig. S5 a-d**). Low MR-PDFF values indicate the presence of brown fat, whereas high MR-PDFF values indicate WAT. Water/fat MSOT images revealed a layered structure consistent with skin, subcutaneous fat and deeper seated muscle and fat tissues. An MSOT fat fraction (FF) was computed (**see Suppl. S5**) from the area expected to contain BAT and WAT, in analogy to the MR-PDFF. MSOT-FF changes observed from the BAT/WAT area in different volunteers (**see Fig. Suppl. S5f,i**) corresponded to changes in vascularization and water content between BAT and WAT (**see Fig. Suppl. S5. g, j**). Areas of low MSOT-FF were accompanied by a corresponding increase in vascular volume, consistent with the presence of BAT. Conversely, volunteers with high MSOT-FF and low Hb/HbO_2 signals indicated relative absence of BAT, in favor

of WAT. Even if MSOT and MRI images were not accurately co-registered in the study, but only approximately obtained from the same volume, we correlated MSOT-FF to MR-DPFF values and found a positive correlation with correlation coefficient of r=0.56 (p = 0.003) (**suppl. Fig. S5 k**).

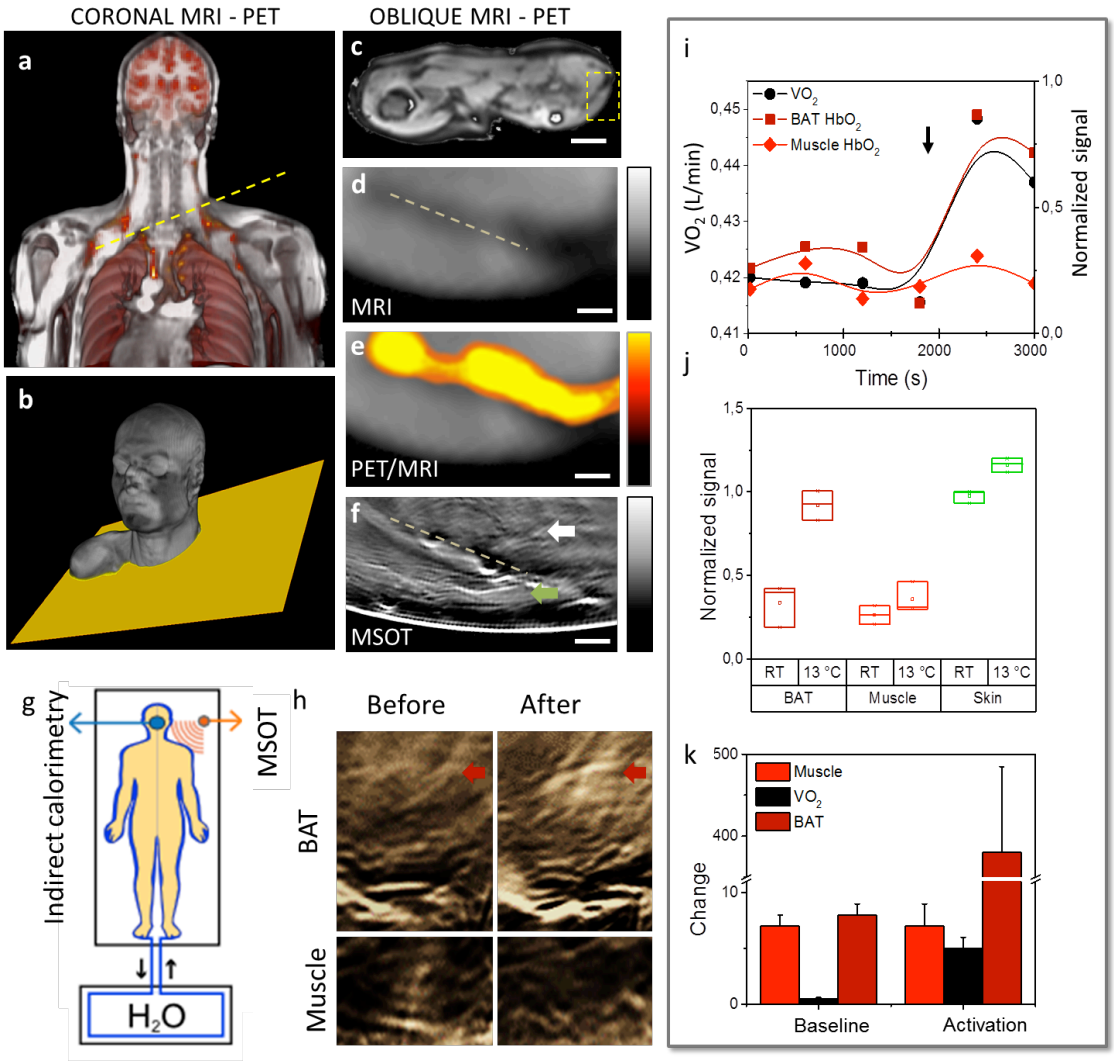

Figure 4: Handheld MSOT of human volunteers. (a) MRI – PET coronal co-registration of the upper torso of a volunteer; the MSOT imaging plane is indicated by the yellow dotted line. (b) 3D MRI rendering of (a), with the MSOT imaging angle indicated as a yellow plane. (c) Oblique MRI slice of the shoulder region along the yellow plane in (b). (d) MRI image of the supraclavicular region shown in (c) as a dotted-line box. (e) Registration of the corresponding PET signal (color) on (d), showing ^{18}F-FDG uptake in activated BAT. (f) MSOT handheld image from the same region as in (d), showing BAT (white arrow) and muscle (green arrow). (g) Schematic of simultaneous indirect calorimetry and MSOT measurements of cold activation using 13 °C water. (h) Before and after cold activation, MSOT was used to image BAT and muscle areas indicated on (f) with white and green arrows, respectively. (i) HbO_2 signals from BAT and muscle, and corresponding $\dot{V}O2$ measurements over the time recorded. The black arrow indicates the beginning of cold exposure. (j) Relative changes of signal intensity in BAT, muscle and skin before and 10 min after cold exposure. (k) Comparative percentage change between baseline (baseline 0 – 1800 s) and baseline plus activation (activation 0 – 3000 s) in muscle, $\dot{V}O2$ and BAT ROIs (n = 3). Scale bars, 5 cm (c), 5 mm (d,e,f) and 1 mm (f) (*p < 0.05).

Discussion

Besides its thermoregulatory function, BAT is implicated in energy homeostasis due to its ability to combust high amounts of nutrient energy (27, 28). In humans, a negative correlation between BAT activity after cold exposure and BMI and fat mass was demonstrated (4, 29). These observations have directed investigations that aim to alter BAT mass and activity to counteract energy imbalance (30). In such studies, quantitative measurements of BAT metabolism can radically complement generic weight gain/loss or body composition measurements by providing observations of the effects of substances, drugs and environmental factors on metabolism *in vivo*.

Overall, the development of *label-free* non-ionizing radiation methods for non-invasive quantitative measurement of energy expenditure can change the landscape of studying metabolism in BAT and other tissues *in vivo*. A critical step toward this direction is achieved by the development of handheld MSOT (31, 32), which yielded herein accurate spectral measurements of metabolic readings. Even though hemoglobin has long been recognized as a source of contrast for near-infrared spectroscopy (NIRS) and diffuse optical tomography (DOT) (33), the poor resolution of these techniques has limited the accuracy and the range of reliable applications (34). Hemoglobin is also employed in optoacoustic (photoacoustic) imaging to visualize blood vessels and micro-vasculature (32, 35). Conversely, by applying *macroscopic* optoacoustic imaging in the near-infrared (NIR), we resolved not only vasculature but also general tissue features and related for the first time high-resolution tissue hemoglobin readings in metabolic measurements of brown fat, confirmed by indirect calorimetry. Imaging of tissue HbO_2 and Hb was achieved by employing key technology advances. First, curved detector arrays significantly improve image quality over linear arrays clinically applied in the past and allowed morphological imaging of tissue structures in mice and humans. Second, we employed detectors custom-designed for optoacoustic imaging, which allowed broader frequency-band detection over conventional ultrasound arrays, typically manufactured for operation in narrow bandwidths. Third, the acquisition of one cross-sectional frame per laser-pulse and wavelength, based on a new class of fast-switch lasers, and advanced image-reconstruction models enabled motion-free

accurate image reconstructions and, importantly, allowed the seamless use of an extended spectral range (700-970 nm) within seconds of scan times, which yielded simultaneous reconstructions of Hb, HBO_2, lipid and water tissue content.

Capitalizing on above-mentioned advances in imaging performance, MSOT resolved BAT activation in mice and humans. MSOT separated oxy- and deoxy-hemoglobin in high resolution, computed SO_2 and TBV values and further unmixed fat and water based on a non-invasive, handheld modality which operates with non-ionizing radiation and in label-free mode. Compared to ^{18}F-FDG-PET, the current gold standard for imaging metabolic activity, MSOT is shown to open new possibilities for BAT and possibly other tissue metabolism measurements by allowing label-free, handheld (portable), longitudinal and disseminated operation, without the need to use radio-isotopes. These features are not offered by any other radiological method today.

Oxygen consumption is an indirect but definitive measure of aerobic metabolism, supported by an increase in blood flow reflecting greater oxygen demand (13, 14). SO_2 and TBV values of activated BAT strongly correlated with indirect calorimetry measurements in mice and IC and PET in humans, showing timing differences compared to the corresponding HbO_2 and Hb signals. To assess dynamic tissue responses we also computed SO_2 and TBV rates (time gradients). While the SO_2 value statically reveals the tissue oxygenation state at a given time point, the SO_2 rate is proposed as a more precise marker of oxygen consumption. Likewise the TBV rate is proposed as a measure of blood volume influx (tissue perfusion). BAT activation was manifested by a corresponding increase in SO_2 rate (Fig. 3e) and an initially positive blood flow (BAT perfusion; Fig. 3f), which subsequently becomes negative when tissue oxygen demand is met. In the future, a higher sampling rate may allow a more precise determination of SO_2 and TBV rates, possibly revealing a more detailed picture of the temporal evolution of BAT activation.

IC was employed herein as the gold-standard for the analysis of energy expenditure in rodents (5, 39, 40), and was also considered for the validation of human measurements based on correlative $\dot{V}O_2$ monitoring. Computed TBV and SO_2 values exhibited a 4-fold stronger local SO_2 change in brown fat over a global VO_2 value, also recorded as a SO_2 change in the Sulzer Vein (**see suppl. Fig. S3 g**). This finding indicates that MSOT may provide a more accurate measurement of metabolism than IC, since the optoacoustic method measures tissue responses in a localized fashion, whereby IC records activity in a delayed and global fashion.

In addition to recording activation and metabolic changes, MSOT was also shown capable to identify imaging features associated with BAT morphology. Perfused BAT showed a substantially different spectrum from WAT, possibly explained by the higher content of mitochondria, leading to the characteristic darker brownish color, in contrast to the lighter white or yellow appearance of WAT (38). While these differences are expected within the visible spectrum, we showed that spectral differences also exist in the NIR. Furthermore, BAT exhibited a 2-fold higher overall intensity than WAT (Fig. 1), possibly due to a combination of the different spectral profiles and the profuse BAT vascularization over WAT, a feature confirmed in mice and humans (see **Suppl. Fig. S5. j**). Conversely, the iBAT region of diabetic mice exhibited a weaker intensity (~20% decrease) compared to healthy controls (**suppl. Fig. 3S**). In contrast to ^{18}F-FDG-PET studies, the localization of brown fat is achieved without the need for contrast agents or cold-activation (26). Moreover, spectral interrogation at the 900-970 nm window enabled unmixing of fat and water contributions, which offered a previously undisclosed look into MSOT imaging features in terms of water and fat composition in subcutaneous and BAT/WAT-related lipid content. Reduced lipid content in the BAT area was congruent with increased vascularization seen on the 700-900nm MSOT images and consistent with BAT anatomy and physiology. Different MSOT metrics (SO_2, TBV, HBO_2, fat or water) could be contrasted to MRI measurements. In a pilot investigation we derived an MSOT fat fraction and demonstrated a statistically significant, positive correlation between MSOT-FF and MR-

449 derived proton density fat fraction (PDFF). This correlation is striking given that the MSOT and MR
450 images are not rigorously co-registered but only approximately obtained from the same tissue area.
451
452 Even though BAT metabolism was a primary focus herein, MSOT may be more generally
453 applied to a larger range of applications spanning exercise physiology, bio-energetic/obesity-related
454 studies and different metabolic diseases such as metabolic syndrome, mitochondrial diseases and
455 disorders of lipid metabolism. By enabling longitudinal, point-of-care, or even possibly measurements
456 based on wearable sensors, the method could support scientific research well beyond the limitations
457 set by the complexity of radio-isotope production, the short lifetimes of radio-isotopes and the
458 frequency of the measurement performed. Nevertheless, *in vivo* MSOT is limited to 2-3 cm
459 penetration depth, therefore we anticipate its use primarily in small animals and specific human
460 interrogations. The safe use and ability to expand routine MSOT use to outpatient care may enable the
461 study of metabolism in a personalized manner.
462

Methods

Animals

The mouse *in vivo* experiments were approved by the government of Upper Bavaria (Az.: 55.2-1-54-2532-123-13). Female nude mice (10 - 12 weeks old Nude-1 Foxn1; Harlan Laboratories, Germany) were kept at 24±1°C and fed with standard rodent diet (Altromin 1314, Altromin Spezialfutter GmbH & Co, Germany) with free access to water. They were kept on a 12:12-h light-dark cycle. In addition, a conventional diabetes animal model was employed by administering streptozocin (Sigma, Germany) at 150 mg/kg body weight to male BALB/c mice (6 - 8 weeks old; Harlan Laboratories, Germany) via i.p. injection after 4 – 6 hours fasting.

Multi-spectral Optoacoustic Tomography

Animal MSOT measurements (**suppl. Fig. S1a**) were conducted with a 256-channel real-time imaging MSOT scanner (41) (inVision 256-TF, iThera Medical GmbH, Munich, Germany) using a tunable (680-950 nm) pulsed (<10 ns) optical parametric oscillator laser with a 10 Hz repetition rate. A fiber bundle split in 10 output arms was used for homogeneous light delivery to the imaged sample along a line illumination around the animal body (ring-shaped illumination). Optoacoustic signals were simultaneously acquired by a 256-element, cylindrically focused transducer array covering a solid angle of 270° around the imaged object. The individual detector elements were manufactured from piezocomposite material and had a central frequency of 5 MHz. The system can acquire cross-sectional (transverse) images through phantoms or small animals like mice. A moving stage enables the imaging of different planes, while the illumination and detection devices remain static.

For human measurements we utilized a previously unpublished MSOT handheld scanner (see **suppl. Fig. S1b**). The scanner was based on a 4.5-cm radius semi-circular detector interfaced to human tissue through a water-containing chamber. The illumination source system was similar to that used in the animal system but was operating with 50 Hz scan rate to enable real-time spectral

measurements. The handheld device was engineered capable of providing cross-sectional MSOT images with only a single pulse, thus avoiding the need for averaging. Single-shot imaging enables video rate measurements and fast multi-wavelength measurements, necessary for minimizing motion artifacts and ensuring the acquisition of high-quality images.

Indirect calorimetry

Oxygen consumption for each mouse was analyzed continuously during MSOT scanning using a transportable O_2 analyzer (FoxBox, Sable Systems International, USA). Air at atmospheric pressure was supplied by means of a compressed air bottle reservoir. For the analysis of gas concentrations, air was pulled through the MSOT sample holder using the pump included in the FoxBox respirometry system with a flow rate of 800 ml/min. After leaving the sample holder, air was dehumidified by passing through a cooling trap and then a tube with magnesium perchlorate (Merck KGaA, Germany). Air was then filtered (Model 9922-11, Parker Balston) before entering the O_2 analyzer (**suppl. Fig. S1a**). To correct for drift in the data, the air was pulled through the empty animal holder before and after the analysis of the mouse (baseline measurement). Drift correction was performed using the software ExpeData, which was also used for data recording (ExpeData version 1.1.22, Sable Systems International, USA). Data were collected in 1-sec intervals. Oxygen consumption ($\dot{V}O_2$) of the mouse was calculated according to the following equation (42): $\dot{V}O_2$ [ml/h] = Δvol%O_2* 10* flow [l/h].

Mouse MSOT measurements ex vivo

Ex vivo measurements were performed to measure BAT and WAT spectra and interrogate whether these two different types of tissue could be spectrally separated in tissue-mimicking phantoms. Interscapular BAT and inguinal WAT from the hind limb were collected from mice, perfused with 5 ml PBS and inserted into 3-mm diameter plastic tubes. The 3-mm tubes were then embedded into a 2-cm diameter cylindrical phantom made of 1.3% agar (Sigma-Aldrich, St. Louis, MO, USA) and 6% intralipid emulsion (Sigma-Aldrich, St. Louis, MO, USA), leading to an optically diffusive medium with acoustic properties similar to those of tissue. The use of diffusive phantoms enables better simulation of the geometry, illumination conditions, and acoustic detection conditions expected *in vivo*

518 (43). Imaging was performed at 25 wavelengths in the range 700 nm - 900 nm in steps of 10 nm. For
519 referencing purposes, a previously characterized tube containing India ink was also measured. The ink
520 solution yielded an optical density of 0.5, as determined by a spectrophotometer.
521
522 *Mouse MSOT measurements in vivo*
523 Mice were anesthetized by i.p. injection of 75 mg/kg pentobarbital and placed in the MSOT sample
524 holder as described earlier (44). In brief, all animals were placed onto a thin, clear, polyethylene
525 membrane and positioned in the water bath maintained at 34 °C, which provided acoustic coupling and
526 maintained animal temperature while imaging. For imaging BAT activation, norepinephrine
527 (arterenol®, Sanofi, Germany; 1 mg/kg (10)) was injected via a catheter inserted in the tail vein. A
528 total of six animals were used for the activation experiments. Three control animals were injected with
529 saline (0.9 % NaCl). In each measurement, 10 wavelengths spanning 700 nm to 900 nm were acquired
530 in 20-nm steps. The duration of anesthesia and MSOT acquisition was limited to ~2500 sec to ensure
531 ethical animal treatment.
532
533 *Cryoslicing*
534 After imaging, the mice were euthanized with a lethal dose of pentobarbital and frozen to -50°C. The
535 upper torso including the neck was embedded in O.C.T (TissueTeck; Sakura Finetek, USA) and was
536 transversely cryosliced with a step of 50 micrometers using a modified cryotome (CM 1950; Leica
537 Microsystems, Germany) equipped with a CCD camera. The camera was used to capture RGB color
538 images of the surface of the bulk sample remaining after each slicing cycle (21).
539
540 *Model-based reconstruction and data analysis*
541 A model-based tomographic reconstruction method, previously described (45), was employed for
542 MSOT image formation. Optoacoustic images obtained at different wavelengths were then linearly
543 unmixed for oxy- (HbO_2) and deoxygenated (Hb) hemoglobin (in the 700-900nm) and fat and water
544 (in the 900-970, when available). Hemoglobin values were normalized against the maximum HbO_2

value measured in an artery selected for normalization purposes. The data analysis further consisted of the calculation of the total blood volume (TBV = HbO_2 + Hb) and the oxygen saturation (SO_2 = HbO_2 / TBV), the latter closely relating to tissue oxygenation and metabolic changes over time. SO_2 was also calibrated based on an artery signal, assumed to reflect 100% oxygen saturation. SO_2 and TBV rates were drawn by calculating the 1st derivative of the SO_2 and TBV over time. Calculation of activation areas (contour maps; **suppl. Fig. S3 a-d**) was based on discretizing the HbO_2 and Hb images, before and after activation, down to 5 intensity levels.

MSOT handheld measurements and indirect calorimetry in human subjects

^{18}F-FDG-PET and MRI data (Biograph mMR; Siemens Healthcare, Germany) from three subjects were acquired at 70-158 min after the injection of 320-408 MBq ^{18}F-FDG. MRI images were co-registered on the PET images using fiduciary markers. To visualize BAT and measure its activation in humans, a handheld MSOT was used as described previously (41, 46). The handheld MSOT illumination was provided by a tunable pulsed laser (Spitlight 600 OPO, Innolas Laser GmbH, Germany) capable of wavelength tuning (675-1064 nm) on a per-pulse basis at 10 Hz repetition rate. The light was coupled into a fiber bundle (CeramOptec GmbH) with rectangular output size of 40-by-1 mm² to create a line illumination. For detection, a multi-element piezoelectric transducer was used with 256 elements placed in a half arc of 120-mm diameter and central frequency of 5 MHz.

For BAT activation measurements, three subjects wore a cooling suit (EOD cooling suit with pump assembly, Holdfast Systems, ZA). The cooling suit comprises a one-piece garment covering the upper body, upper arms and legs, as well as a close-fitting, open-faced hood for the head as well as a cooling pump that circulates ice-cooled water (4°C) through hoses integrated in the garment. During MSOT handheld imaging, the oxygen consumption of the subjects was analyzed continuously using an exercise physiology kit (ML3508B80 Exercise Physiology System, ADInstruments, NZ). IC data were collected at a rate of 1000 Hz and analyzed by LabChart software (LabChart7 version v.7.2, ADInstruments, NZ) to calculate the oxygen consumption ($\dot{V}O_2$ [L/min]), which is presented as a moving average over 20 points.

MRI –MSOT correlation in human subjects

Twenty-six healthy adult volunteers (10 male, 16 female, mean age, 33.4) were recruited prospectively. Subjects underwent an MRI of the neck region on a 3T scanner (Ingenia, Philips Healthcare). For measuring the supraclavicular proton density fat fraction (PDFF) (36, 47), a six-echo multi-echo gradient echo sequence with bipolar gradients was used with TR = 12 ms, TE1 = 1.24 ms, ΔTE = 1.0, flip angle = 5°, bandwidth = 1413 Hz/pixel, 268x200x93 acquisition matrix size, FOV = 400x300x140 mm^3, 1.5-mm isotropic voxel size, and SENSE with R = 2.5. PDFF maps were generated using the online complex-based fat quantification algorithm, accounting for known confounding factors including the presence of multiple fat peaks, a single T2* correction and phase errors (36, 37, 47, 48). A custom-built MATLAB algorithm was used for delineating the left deep supraclavicular fat pocket and determining the mean supraclavicular PDFF.

MSOT images of approximately the same region were recorded in an extended 700-970 nm spectral region, with the same system discussed in the previous section. ROIs from supraclavicular regions expected to contain BAT or WAT were employed to unmix fat content (presence of fat spectral intensity in total MSOT spectrum) and water content (presence of water spectral intensity in total MSOT spectrum), utilizing the 900-970nm spectral window, which contains prominent absorption contributions from lipids and water. Then the MSOT fat fraction (MSOT-FF) was computed as the fat spectral intensity over fat and water spectral intensity. Statistical analysis was performed by using a t-test, two-tailed and considered as paired samples (type 1). A p-value of < 0.05 was considered as statistically significant.

Acknowledgment

The authors would like to thank Uwe Klemm, Sarah Glasl and Florian Jurgeleit for technical support.

The research leading to these results has received funding by the Deutsche Forschungsgemeinschaft (DFG), Sonderforschungsbereich-824 (SFB-824), subproject A1 and (KL 973/11-1). This work was supported by the Helmholtz cross-program topic “Metabolic Dysfunction”. We furthermore

599 acknowledge funding by the ERC Advanced Grant (233161) Next Generation *in vivo* imaging
600 platform for post-genome biology and medicine MSOT and funding by EU FP7 project DIABAT
601 (HEALTH-F2-2011-278373). DCK aknowledges ERC Starting Grant (grant agreement No 677661,
602 ProFatMRI)

603

604 References

605 1. Cannon B & Nedergaard J (2004) Brown adipose tissue: function and physiological
606 significance. *Physiological reviews* 84(1):277-359.
607 2. Klingenspor M (2003) Cold-induced recruitment of brown adipose tissue thermogenesis.
608 *Experimental physiology* 88(1):141-148.
609 3. Nedergaard J, Bengtsson T, & Cannon B (2007) Unexpected evidence for active brown
610 adipose tissue in adult humans. *American journal of physiology. Endocrinology and*
611 *metabolism* 293(2):E444-452.
612 4. van Marken Lichtenbelt WD*, et al.* (2009) Cold-activated brown adipose tissue in healthy
613 men. *The New England journal of medicine* 360(15):1500-1508.
614 5. Cannon B & Nedergaard J (2011) Nonshivering thermogenesis and its adequate measurement
615 in metabolic studies. *The Journal of experimental biology* 214(Pt 2):242-253.
616 6. Smith RE & Roberts JC (1964) Thermogenesis of Brown Adipose Tissue in Cold-Acclimated
617 Rats. *The American journal of physiology* 206:143-148.
618 7. Nnodim JO & Lever JD (1988) Neural and vascular provisions of rat interscapular brown
619 adipose tissue. *The American journal of anatomy* 182(3):283-293.
620 8. Nicholls DG & Locke RM (1984) Thermogenic mechanisms in brown fat. *Physiological*
621 *reviews* 64(1):1-64.
622 9. Golozoubova V*, et al.* (2001) Only UCP1 can mediate adaptive nonshivering thermogenesis in
623 the cold. *FASEB journal : official publication of the Federation of American Societies for*
624 *Experimental Biology* 15(11):2048-2050.
625 10. Meyer CW*, et al.* (2010) Adaptive thermogenesis and thermal conductance in wild-type and
626 UCP1-KO mice. *American journal of physiology. Regulatory, integrative and comparative*
627 *physiology* 299(5):R1396-1406.
628 11. Bauwens M*, et al.* (2014) Molecular imaging of brown adipose tissue in health and disease.
629 *European journal of nuclear medicine and molecular imaging* 41(4):776-791.
630 12. Foster DO & Frydman ML (1978) Nonshivering thermogenesis in the rat. II. Measurements of
631 blood flow with microspheres point to brown adipose tissue as the dominant site of the
632 calorigenesis induced by noradrenaline. *Canadian journal of physiology and pharmacology*
633 56(1):110-122.
634 13. Foster DO & Frydman ML (1979) Tissue distribution of cold-induced thermogenesis in
635 conscious warm- or cold-acclimated rats reevaluated from changes in tissue blood flow: the
636 dominant role of brown adipose tissue in the replacement of shivering by nonshivering
637 thermogenesis. *Canadian journal of physiology and pharmacology* 57(3):257-270.
638 14. Puchalski W, Bockler H, Heldmaier G, & Langefeld M (1987) Organ blood flow and brown
639 adipose tissue oxygen consumption during noradrenaline-induced nonshivering thermogenesis
640 in the Djungarian hamster. *The Journal of experimental zoology* 242(3):263-271.
641 15. Mirbolooki MR, Constantinescu CC, Pan ML, & Mukherjee J (2011) Quantitative assessment
642 of brown adipose tissue metabolic activity and volume using 18F-FDG PET/CT and β3-
643 adrenergic receptor activation. *EJNMMI research* 1(1):30.

16. Ouellet V*, et al.* (2012) Brown adipose tissue oxidative metabolism contributes to energy expenditure during acute cold exposure in humans. *The Journal of clinical investigation* 122(2):545-552.
17. Chen YI*, et al.* (2012) Anatomical and functional assessment of brown adipose tissue by magnetic resonance imaging. *Obesity* 20(7):1519-1526.
18. Nakayama A, Bianco AC, Zhang CY, Lowell BB, & Frangioni JV (2003) Quantitation of brown adipose tissue perfusion in transgenic mice using near-infrared fluorescence imaging. *Molecular imaging* 2(1):37-49.
19. Crane JD, Mottillo EP, Farncombe TH, Morrison KM, & Steinberg GR (2014) A standardized infrared imaging technique that specifically detects UCP1-mediated thermogenesis in vivo. *Molecular metabolism* 3(4):490-494.
20. Ntziachristos V & Razansky D (2010) Molecular imaging by means of multispectral optoacoustic tomography (MSOT). *Chemical reviews* 110(5):2783-2794.
21. Tzoumas S*, et al.* (2014) Immune cell imaging using multi-spectral optoacoustic tomography. *Optics letters* 39(12):3523-3526.
22. Granneman JG, Burnazi M, Zhu Z, & Schwamb LA (2003) White adipose tissue contributes to UCP1-independent thermogenesis. *American journal of physiology. Endocrinology and metabolism* 285(6):E1230-1236.
23. Ohlson KB, Mohell N, Cannon B, Lindahl SG, & Nedergaard J (1994) Thermogenesis in brown adipocytes is inhibited by volatile anesthetic agents. A factor contributing to hypothermia in infants? *Anesthesiology* 81(1):176-183.
24. Dicker A, Cannon B, & Nedergaard J (1995) Cold acclimation-recruited nonshivering thermogenesis: the Syrian hamster is not an exception. *The American journal of physiology* 269(4 Pt 2):R767-774.
25. Ohlson KB, Lindahl SG, Cannon B, & Nedergaard J (2003) Thermogenesis inhibition in brown adipocytes is a specific property of volatile anesthetics. *Anesthesiology* 98(2):437-448.
26. Wu C*, et al.* (2014) Activating brown adipose tissue for weight loss and lowering of blood glucose levels: a microPET study using obese and diabetic model mice. *PloS one* 9(12):e113742.
27. Rothwell NJ & Stock MJ (1979) A role for brown adipose tissue in diet-induced thermogenesis. *Nature* 281(5726):31-35.
28. Himms-Hagen J (1979) Obesity may be due to a malfunctioning of brown fat. *Canadian Medical Association journal* 121(10):1361-1364.
29. Saito M*, et al.* (2009) High incidence of metabolically active brown adipose tissue in healthy adult humans: effects of cold exposure and adiposity. *Diabetes* 58(7):1526-1531.
30. Vijgen G & van Marken Lichtenbelt W (2013) Brown adipose tissue: clinical impact of a re-discovered thermogenic organ. *Frontiers in bioscience* 5:823-833.
31. Buehler A, Kacprowicz M, Taruttis A, & Ntziachristos V (2013) Real-time handheld multispectral optoacoustic imaging. *Optics letters* 38(9):1404-1406.
32. Taruttis A & Ntziachristos V (2015) Advances in real-time multispectral optoacoustic imaging and its applications. *Nat Photon* 9(4):219-227.
33. Ntziachristos V, Ripoll J, Wang LV, & Weissleder R (2005) Looking and listening to light: the evolution of whole-body photonic imaging. *Nature biotechnology* 23(3):313-320.
34. Ntziachristos V (2010) Going deeper than microscopy: the optical imaging frontier in biology. *Nature methods* 7(8):603-614.
35. Wang LV & Hu S (2012) Photoacoustic tomography: in vivo imaging from organelles to organs. *Science* 335(6075):1458-1462.
36. Hu HH & Kan HE (2013) Quantitative proton MR techniques for measuring fat. *NMR in biomedicine* 26(12):1609-1629.
37. Karampinos DC*, et al.* (2014) Bone marrow fat quantification in the presence of trabecular bone: initial comparison between water-fat imaging and single-voxel MRS. *Magnetic resonance in medicine* 71(3):1158-1165.
38. Anonymous (!!! INVALID CITATION !!!).

39. Tschop MH*, et al.* (2012) A guide to analysis of mouse energy metabolism. *Nature methods* 9(1):57-63.
40. Even PC & Nadkarni NA (2012) Indirect calorimetry in laboratory mice and rats: principles, practical considerations, interpretation and perspectives. *American journal of physiology. Regulatory, integrative and comparative physiology* 303(5):R459-476.
41. Dima A, Burton NC, & Ntziachristos V (2014) Multispectral optoacoustic tomography at 64, 128, and 256 channels. *Journal of biomedical optics* 19(3):36021.
42. Heldmaier G & Ruf T (1992) Body temperature and metabolic rate during natural hypothermia in endotherms. *Journal of comparative physiology. B, Biochemical, systemic, and environmental physiology* 162(8):696-706.
43. Vonnemann J*, et al.* (2014) Polyglycerolsulfate functionalized gold nanorods as optoacoustic signal nanoamplifiers for in vivo bioimaging of rheumatoid arthritis. *Theranostics* 4(6):629-641.
44. Razansky D, Buehler A, & Ntziachristos V (2011) Volumetric real-time multispectral optoacoustic tomography of biomarkers. *Nature protocols* 6(8):1121-1129.
45. Rosenthal A, Razansky D, & Ntziachristos V (2010) Fast semi-analytical model-based acoustic inversion for quantitative optoacoustic tomography. *IEEE transactions on medical imaging* 29(6):1275-1285.
46. Diot G, Dima A, & Ntziachristos V (2015) Multispectral opto-acoustic tomography of exercised muscle oxygenation. *Optics letters* 40(7):1496-1499.
47. Baum T*, et al.* (2016) MR-based assessment of body fat distribution and characteristics. *European journal of radiology* 85(8):1512-1518.
48. Karampinos DC, Yu H, Shimakawa A, Link TM, & Majumdar S (2011) T(1)-corrected fat quantification using chemical shift-based water/fat separation: application to skeletal muscle. *Magnetic resonance in medicine* 66(5):1312-1326.